AGU PUBLICATIONS

JGR

Journal of Geophysical Research: Oceans

RESEARCH ARTICLE

10.1002/2014JC010221

Key Points:
- The ocean's interior can be retrieved from surface data
- The isQG method could serve as a simplified dynamic framework
- The isQG method can be applied to the satellite-derived data

Correspondence to:
S. Peng,
speng@scsio.ac.cn

Citation:
Liu, L., S. Peng, J. Wang, and R. X. Huang (2014), Retrieving density and velocity fields of the ocean's interior from surface data, *J. Geophys. Res. Oceans*, *119*, 8512–8529, doi:10.1002/2014JC010221.

Received 5 JUN 2014
Accepted 25 NOV 2014
Accepted article online 28 NOV 2014
Published online 12 DEC 2014

Retrieving density and velocity fields of the ocean's interior from surface data

Lei Liu[1,2], Shiqiu Peng[1], Jinbo Wang[3], and Rui Xin Huang[4]

[1]State Key Laboratory of Tropical Oceanography, South China Sea Institute of Oceanology, Chinese Academy of Sciences, Guangzhou, China, [2]University of Chinese Academy of Sciences, Marine Science, Beijing, China, [3]Scripps Institution of Oceanography, University of California, San Diego, La Jolla, California, USA, [4]Woods Hole Oceanographic Institution, Woods Hole, Massachusetts, USA

Abstract Using the "interior + surface quasigeostrophic" (isQG) method, the density and horizontal velocity fields of the ocean's interior can be retrieved from surface data. This method was applied to the Simple Ocean Data Assimilation (SODA) and the Hybrid Coordinate Ocean Model (HYCOM)/Navy Coupled Ocean Data Assimilation (NCODA) reanalysis data sets. The input surface data include sea surface height (SSH), sea surface temperature (SST), sea surface salinity (SSS), and a region-averaged stratification. The retrieved subsurface fields are compared with reanalysis data for three tested regions, and the results indicate that the isQG method is robust. The isQG method is particularly successful in the energetic regions like the Gulf Stream region with weak stratification, and the Kuroshio region with strong correlation between sea surface density (SSD) and SSH. It also works, though less satisfactorily, in the Agulhas leakage region. The performance of the isQG method in retrieving subsurface fields varies with season, and peaks in winter when the mixed layer is deeper and stratification is weaker. In addition, higher-resolution data may facilitate the isQG method to achieve a more successful reconstruction for the velocity retrieval. Our results suggested that the isQG method can be used to reconstruct the ocean interior from the satellite-derived SSH, SST, and SSS data in the near future.

1. Introduction

During the past decades, advances in satellite technology have greatly improved our understanding of the ocean circulation and variability by providing spatially and temporally well-sampled sea surface information, including sea surface height (SSH), temperature (SST), and salinity (SSS) with a global coverage. Because the in situ observations beneath the sea surface are still sparse, a method that projects the high-resolution satellite sea surface information to the ocean interior becomes invaluable for a better understanding of the interior ocean circulation and dynamics.

Great efforts have been made to retrieve the ocean's interior fields using satellite-derived sea surface data. Because the variation in sea surface height mostly reflects the movement of interior thermocline, there exists a significant statistical relationship between SSH and interior temperature and salinity fields. *Carnes et al*. [1990, 1994] reconstructed the subsurface temperature and salinity fields using a regression relationship between surface dynamical height and the amplitudes of empirical orthogonal functions (EOFs) for the vertical temperature structure. *Watts et al*. [2001] constructed a "gravest empirical mode" (GEM) based on a large assemblage of historical hydrographic data along the WOCE SR3 transect south of Australia and demonstrated that more than 96% variance in the temperature and salinity fields between 150 and 3000 dbars can be captured by GEM representation.

While statistical methods can provide quite satisfactory subsurface information based on sufficient historical statistics, dynamical methods can provide dynamically consistent fields without relying on the availability of local historical data. Based on ocean model dynamics, *Hurlburt* [1986] used surface pressure to calculate the corresponding subsurface structure in a simple two-layer primitive model. *Haines* [1991] assimilated altimeter data using a four-layer quasigeostrophic (QG) model and assuming the subsurface potential vorticity (PV) was conserved at assimilation time. The scope of the work by *Haines* [1991] was greatly extended by *Cooper and Haines* [1996] using a full nonadiabatic and multilevel model in a twin experiment framework.

Surface data, such as SST, can also be assimilated using primitive ocean models [*Chen et al*., 1997; *Rosati et al*., 1997; *Syu and Neelin*, 2000; *Tang and Hsieh*, 2003].

In recent years, more and more attentions have been paid to the surface quasigeostrophic (SQG) theory [*Held et al*., 1995], which could serve as a simplified framework to describe the dynamics of the upper troposphere. The SQG theory was first successfully applied in the atmospheric studies [*Blumen*, 1978; *Juckes*, 1994; *Hakim et al*., 2002; *Tulloch and Smith*, 2006, 2009]. In these studies, the tropopause was treated as a boundary. Potential temperature anomalies on this boundary alone could depict the 3-D dynamics of the upper troposphere.

The SQG theory was also explored within the oceanographic context to determine the influence of sea surface boundary on the dynamics of the upper ocean. The upper ocean, unlike the atmospheric troposphere, has significant interior PV that contributes to surface fields. It is argued that the interior PV is correlated with surface pressure and/or buoyance fields. *Lapeyre and Klein* [2006] developed an "effective" SQG (eSQG) method by adjusting the stratification parameter to account for the missing interior PV. The method has been tested against a simulation of a primitive equation (PE) model with an idealized initial front [*Lapeyre and Klein*, 2006], satellite measurements [*Isern-Fontanet et al*., 2006], and an ocean general circulation simulation [*Isern-Fontanet et al*., 2008], all of which yielded promising results. Similarly, *LaCasce and Mahadevan* [2006] derived interior PV empirically from SST, and modified the SQG model to estimate subsurface fields. A qualitative good agreement was found between in situ measurements and results from the modified SQG method. *Klein et al*. [2008, 2009] suggested that some specific SQG properties could be valid for dynamics involving large Rossby numbers, and applied the SQG frame work to diagnose the vertical velocity field from SSH. *LaCasce* [2012] analyzed the SQG solution using a more realistic (exponential) stratification. These methods assume that the surface density and interior PV are correlated, in which case SSH would have the same phase with the sea surface density (SSD). However, SSH and SSD fields are sometimes quite different in real ocean [*Wang et al*., 2013; *González-Haro and Isern-Fontanet*, 2014; *Isern-Fontanet et al*., 2014], indicating the modified form of SQG solution may not capture the vertical shift of the SST and interior PV.

Due to the linearity of the quasigeostrophic PV, the solution can be decomposed into two components: SQG solution and interior solution [*Hoskins*, 1975; *Blumen*, 1978; *Lapeyre and Klein*, 2006; *Ferrari and Wunsch*, 2010]. *Wang et al*. [2013] reexamined SQG dynamics and pointed out that both SQG and interior solutions contribute to the sea surface height (pressure), and thus proposed the "interior + surface QG" (isQG) method to reconstruct the subsurface state from surface fields. In contrast to the SQG method, the isQG method can circumvent the limitation of assuming good correlation between SSH and SSD. As the first step, *Wang et al*. [2013] tested this method in the context of idealized ocean, i.e., using the surface fields from a PE numerical model (the Parallel Ocean Program, POP), to construct the subsurface fields, which were validated against the numerical model output. Results demonstrated that the subsurface fields reconstructed by the isQG method were in agreement with those from the POP model, especially in the regions with energetic eddies, such as the Gulf Stream extension and regions at high latitudes where stratification is weak. The results, though based on idealized oceanic conditions, highlight the potential application of the new isQG method in constructing the interior of the real ocean in the future. With the availability of satellite-derived SSS from SMOS (Soil Moisture and Ocean Salinity)/Aquarius with increasingly improving accuracy, this method seems quite promising. However, there are still some open issues associated with the application of isQG method in practice, such as the seasonal variation of the isQG performance and the impact of data resolution on its performance. In this study, we aim to investigate these issues with a more realistic context using reanalysis data. Because reanalysis data combine ocean observations with the computational model, they can provide a more refined and realistic estimate of the ocean state than the pure model output as those in *Wang et al*. [2013], and thus can make the validation of the isQG method more reliable and robust.

The rest of this paper is organized as follows. The isQG method is briefly reviewed in section 2. The reanalysis data are described in section 3. Section 4 presents the results, and section 5 gives a summary.

2. The isQG Method

The isQG method considers the QG balanced motions in the ocean, describing eddy activities with spatial scales of 10–500 km and temporal scales of 10–150 days [*Charney and Flierl*, 1981]. In the QG theory, the geostrophic stream function of a flow field can be calculated by inversion from a known PV field subjected

to proper boundary conditions [*Bishop and Thorpe*, 1994; *Hoskins et al*., 1985]. Stream function and PV are related by an elliptic operator $\mathcal{L}$:

$$\begin{gathered}\mathcal{L}\Psi = q(x,y,z,t),\\ \mathcal{L}=\left(\frac{\partial^2}{\partial x^2}+\frac{\partial^2}{\partial y^2}+\frac{\partial}{\partial z}\frac{f_0^2}{N^2}\frac{\partial}{\partial z}\right),\quad -H<z<0,\end{gathered} \tag{1}$$

where f_0 is the mean Coriolis parameter in the model domain, N^2 the Brunt-Väisälä frequency, $\Psi=p(\rho_0 f_0)^{-1}$ the stream function, and q the deviation from the large-scale background *PV*. p and ρ_0 in the definition of Ψdenote the pressure anomaly and the reference density, respectively.

Boundary conditions are required to invert (1) to obtain the stream function field. Upper and lower boundary conditions are derived from the QG density equation:

$$\frac{\partial}{\partial z}\Psi(x,y,0,t)=f_0^{-1}b(x,y,0,t), \tag{2}$$

$$\frac{\partial}{\partial z}\Psi(x,y,-H,t)=f_0^{-1}b(x,y,-H,t)=0, \tag{3}$$

where $b=-g\rho/\rho_0$ is the buoyancy anomaly with ρ being the density anomaly. Density anomaly at the seafloor ($z=-H$) is neglected. The domain is subjected to doubly periodic lateral boundary conditions.

Ψ can be calculated as the sum of surface (SQG) solution and interior solution due to the linearity of the QG PV equation [*Hoskins*, 1975; *Lapeyre and Klein*, 2006; *Ferrari and Wunsch*, 2010]. The surface solution is forced by surface buoyancy anomaly and involves zero PV anomaly in the interior, while the interior solution is associated with interior PV anomaly with zero surface buoyancy anomaly. Therefore, we have the following equations and boundary conditions,

$$\Psi^t=\Psi^s+\Psi^i, \tag{4}$$

$$\begin{gathered}\mathcal{L}\Psi^s=0\\ \left.\frac{\partial\Psi^s(x,y,z,t)}{\partial z}\right|_{z=0,\,-H}=\frac{b(x,y,z,t)}{f_0},\end{gathered} \tag{5}$$

$$\begin{gathered}\mathcal{L}\Psi^i=q\\ \left.\frac{\partial\Psi^i(x,y,z,t)}{\partial z}\right|_{z=0,\,-H}=0,\end{gathered} \tag{6}$$

where Ψ^t is the total stream function, Ψ^s the SQG solution, and Ψ^i the interior solution.

In the horizontal Fourier transform domain, equations (5) and (6) simply reduce to the following ordinary differential equations:

$$\begin{gathered}\frac{\partial}{\partial z}\frac{f_0^2}{N^2}\frac{\partial}{\partial z}\hat{\Psi}^s-\kappa^2\hat{\Psi}^s=0\\ \left.\frac{d\hat{\Psi}^s}{dz}\right|_{z=0}=\frac{\hat{b}(k,l,z)}{f_0}\\ \left.\frac{d\hat{\Psi}^s}{dz}\right|_{z=-H}=0,\end{gathered} \tag{7}$$

$$\begin{gathered}\frac{\partial}{\partial z}\frac{f_0^2}{N^2}\frac{\partial}{\partial z}\hat{\Psi}^i-\kappa^2\hat{\Psi}^i=\hat{q}\\ \left.\frac{d\hat{\Psi}^i}{dz}\right|_{z=0,\,-H}=0,\end{gathered} \tag{8}$$

where (k, l) are the horizontal wave numbers and $\kappa=(k^2+l^2)^{1/2}$. The hatted variables are spectral amplitudes. For given sea surface information and stratification, equation (7) can be solved directly.

On the other hand, equation (8) cannot be solved directly because the PV anomaly $\hat{q}$ in the interior ocean is unknown. However, $\hat{\Psi}^i$ can be derived through a different approach based on pressure anomalies on the boundaries and the barotropic-baroclinic modes. Sea surface height (pressure) anomaly and bottom pressure anomaly are reflected by the collective contribution from SQG solution and interior solution:

$$\Psi^t(z=0)=\Psi^s(0)+\Psi^i(0)=\frac{g}{f_0}\eta, \tag{9}$$

$$\Psi^s(-H)+\Psi^i(-H)=0, \tag{10}$$

where η is SSH anomaly. Equation (10) implies that bottom-velocity vanishes. In terms of Fourier transform:

$$\hat{\Psi}^s(k,l,0)+\hat{\Psi}^i(k,l,0)=\frac{g}{f_0}\hat{\eta}(k,l), \tag{11}$$

$$\hat{\Psi}^s(k,l,-H)+\hat{\Psi}^i(k,l,-H)=0. \tag{12}$$

The barotropic-baroclinic modes are the solutions $F_m(z)$ to the following Sturm-Liouville eigenvalue problem [*Pedlosky*, 1987]:

$$\frac{\partial}{\partial z}\left(\frac{f_0^2}{N^2}\frac{\partial F_m}{\partial z}\right)=-R_m^{-2}F_m;\ \frac{dF_m}{dz}=0,\ \ \text{at}\ z=0,-H, \tag{13}$$

where $m \geq 0$ is an integer with $m=0$ denoting the barotropic mode and $m > 0$ the baroclinic modes, R_m the Rossby deformation radius associated with vertical mode m. For given stratification $N^2(z)$, $F_m(z)$ can be solved numerically.

One can project $\hat{\Psi}^i$ onto eigenfunctions F_m, which are orthonormal and form a complete basis,

$$\hat{\Psi}^i(k,l,z)=\sum_n A_n(k,l)F_n(z). \tag{14}$$

Since satellite altimetric signals are largely dominated by the barotropic and first baroclinic modes [*Stammer*, 1997; *Wunsch*, 1997; *Smith and Vallis*, 2001; *Chelton et al.*, 2011], expression (14) can be approximated as the sum of these two modes,

$$\hat{\Psi}^i(k,l,z)=A_0(k,l)F_0(z)+A_1(k,l)F_1(z). \tag{15}$$

Substituting (15) into equations (11) and (12) leads to:

$$A_0F_0(0)+A_1F_1(0)=\frac{g}{f_0}\hat{\eta}-\hat{\Psi}^s(k,l,0), \tag{16}$$

$$A_0F_0(-H)+A_1F_1(-H)=-\hat{\Psi}^s(k,l,-H). \tag{17}$$

With the observed SSH field, $\hat{\Psi}^s$ calculated from equation (7), and $F_m(z)$ obtained from equation (13), amplitudes of the two modes A_0 and A_1 can be determined. Thus, interior solution $\hat{\Psi}^i$ and total stream function Ψ^t can be obtained from equations (14) and (4).

3. Data

3.1. Reanalysis Data Sets

We use two kinds of data assimilation products in this study to evaluate the isQG method, i.e., Simple Ocean Data Assimilation (SODA) and the Hybrid Coordinate Ocean Model (HYCOM)/Navy Coupled Ocean Data Assimilation (NCODA) reanalysis data sets. The SODA reanalysis is a global ocean reanalysis created by assimilating observational data into an ocean general circulation model based on the POP model. The observations assimilated include the historical archive of hydrographic profiles, moored hydrographic observations, remotely sensed SST, altimeter sea level etc. [*Carton and Giese*, 2008]. It provides monthly averaged gridded variables (salinity, temperature, velocity etc.) with a horizontal resolution of $0.5^\circ \times 0.5^\circ$ at

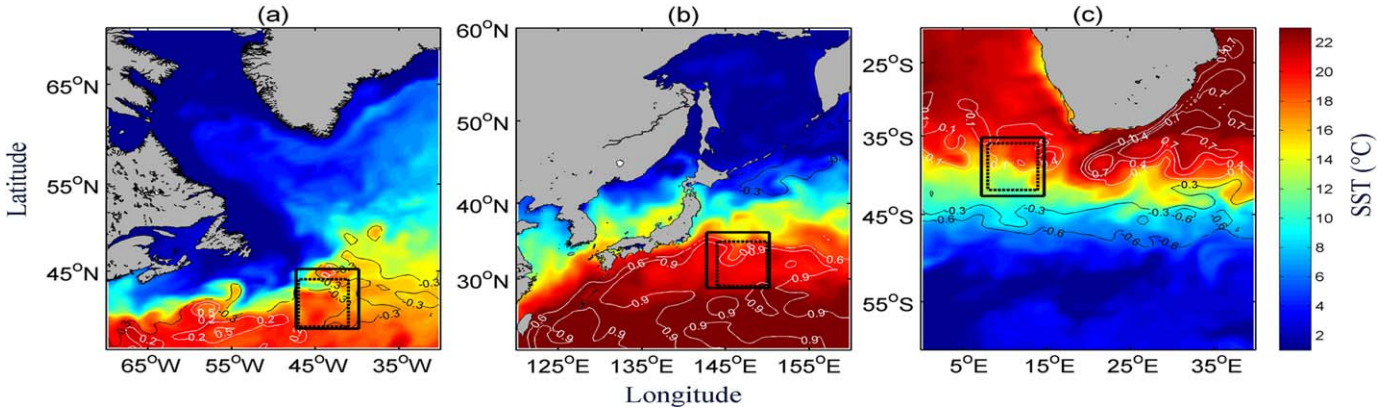

Figure 1. Geographical location of three tested regions marked by black boxes for SODA data (solid), and HYCOM data (dashed). (a) Gulf Stream region (47.25°W–39.75°W, 37.75°N–45.25°N for SODA data; 47°W–41°W, 38°N–44°N for HYCOM data), (b) Kuroshio region (142.75°E–150.25°E, 28.75°N–36.25°N for SODA data; 144°E–150°E, 29°N–35°N for HYCOM data), and (c) Agulhas leakage region (7.25°E–14.75°E, 42.75°S–35.25°S for SODA data; 8°E–14°E, 42°S–36°S for HYCOM data). Fields of SST (color) and SSH (contour) from SODA reanalysis data in January 2007 are overlaid.

40 levels (from −5.01 to −5375 m). The temporal and spatial resolutions are relatively coarse, but the model data still resolves most of mesoscale eddies in our study regions. The HYCOM/NCODA reanalysis (GLBa0.08/expt_90.8) is provided by the ocean forecast model HYCOM [*Chassignet et al*., 2009] using the NCODA system to ingest observations, such as satellite observations (SSH, SST), as well as vertical temperature and salinity profiles from in situ and float measurements (XBTs, Argo floats and moored buoys) [*Cummings*, 2005]. This reanalysis provides three-dimensional ocean state estimates (salinity, temperature, velocity etc.) with high spatial and temporal resolution (1/12°, daily) and 32 vertical layers (from 0 to −5500 m).

Three stamp regions are chosen as the test bed of the isQG solution: the Gulf Stream extension, the Kuroshio system east off Japan, and the Agulhas leakage in the South Atlantic Ocean, with domain sizes of 7.5° × 7.5° (solid boxes in Figure 1) for using SODA data of January 2007 and 6° × 6° (dashed boxes in Figure 1) for using HYCOM/NCODA data of January-December 2010. Due to the denser horizontal grids resulted from the high spatial resolution of HYCOM/NCODA data (1/12°), slightly smaller domain size is used for HYCOM/NCODA data to facilitate computation.

3.2. Data Preprocess

The input of the isQG method includes three variables: sea surface density eddy (anomaly) field (SSDA), sea surface height eddy field (SSHA), and vertical stratification profile$N^2(z)$.

We first derive density, potential density at different levels using temperature and salinity data from SODA data and using the commonly used subroutines based on the UNESCO1983 equation of state [*Fofonoff and Millard*, 1983]. Density field at −5.01 m is treated as a proxy for sea surface density. The area-averaged Brunt-Väisälä frequency $N^2(z)$ is calculated from potential density using the mean pressure between two vertical grids as the reference pressure:

$$N^2 = -\frac{g}{\rho_v}\frac{\partial \bar{\rho}}{\partial z}, \tag{18}$$

where ρ_v is the volumetric mean of potential density, and $\bar{\rho}$ the horizontal mean of potential density in target regions.

$N^2(z)$ deduced above could not be directly applied to the isQG dynamics, because its value approaches zero near the surface (dashed lines in Figures 2a–2c), which can cause unrealistic overshoot of the SQG solution. To solve this problem, we modify the stratification profiles in the ML, using the method applied by *Wang et al*. [2013]: replacing the surface stratification by the mixed-layer-averaged N^2; the linear interpolation between this new surface value and the value at the base of ML (solid lines in Figures 2a–2c) is then substituted as the stratification profile in the ML.

To get eddy fields, we then remove the mean large-scale background information from SSD fields and SSH fields. The background field is calculated through a least square fit of a field to the quadratic surface $S(x, y)$ [*Wang et al*., 2013],

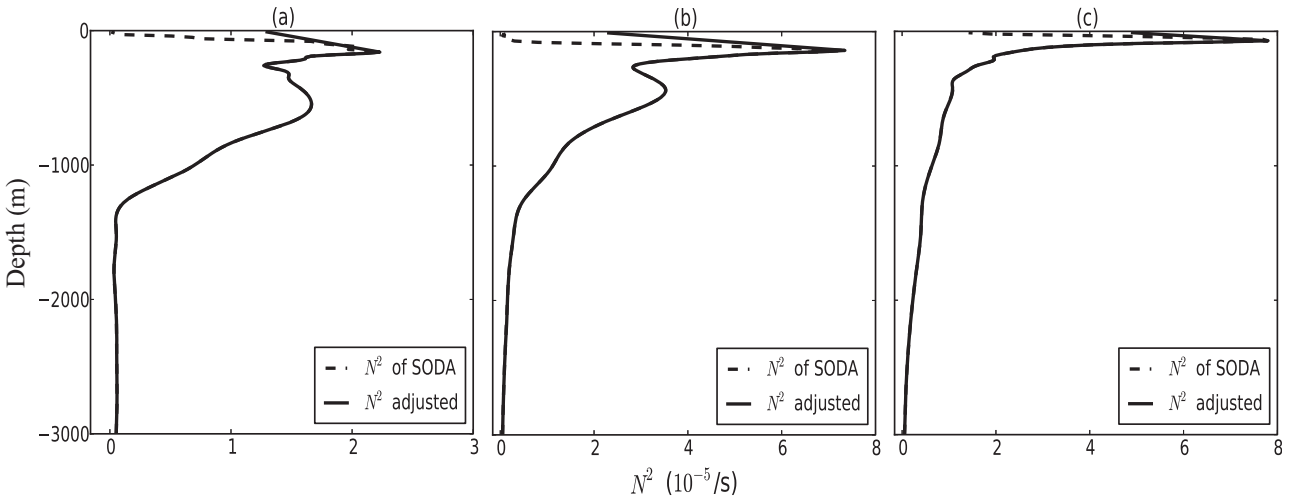

Figure 2. Stratification profiles from SODA (dashed lines), and the adjusted N^2 value used in the isQG method (solid lines) for (a) Gulf Stream region, (b) Kuroshio region, and (c) Agulhas leakage region.

$$S(x,y)=[C_0,C_1,C_2,C_3,C_4,C_5][1,x,y,x^2,y^2,xy]^T, \quad (19)$$

where x and y denote the zonal and meridional coordinates, respectively. Figure 3 gives the SSDA (color) and SSHA (contours) fields in the three tested regions.

HYCOM/NCODA data of the 10–18 days of each month in 2010 are selected to produce 12 groups of 9 day averaged data set. To investigate the sensitivity of the isQG performance to horizontal resolution of data, two data sets with coarser resolutions (0.24° and 0.4°) are generated by subsampling the high-resolution data set (1/12°). The same procedure described above for SODA data is then applied to these three HYCOM/NCODA data sets with different spatial resolution. Note that there is no need of proxy for sea surface variables in HYCOM/NCODA data set because this reanalysis provides variables at the surface (0 m).

We calculate the pressure anomalies at the ocean floor (selected as −3000 m) from both reanalysis data sets and found that they are all nearly zero, which makes the assumption of the zero pressure anomalies at the bottom valid for the isQG reconstruction in this study. Now the isQG is solved numerically given the SSDA, SSHA, and $N^2(z)$. Results are assessed against the original reanalysis data to see if this method is capable of retrieving subsurface fields from the reanalysis data effectively.

4. Results

Results in this section include two variables deduced from the reconstructed geostrophic stream function: eddy field of density $\rho^a=-\frac{\rho_0 f}{g}\frac{\partial\Psi}{\partial z}$, and eddy velocity $\vec{V}=\vec{z}\times\nabla\Psi$. Hereafter, the superscript a means eddy

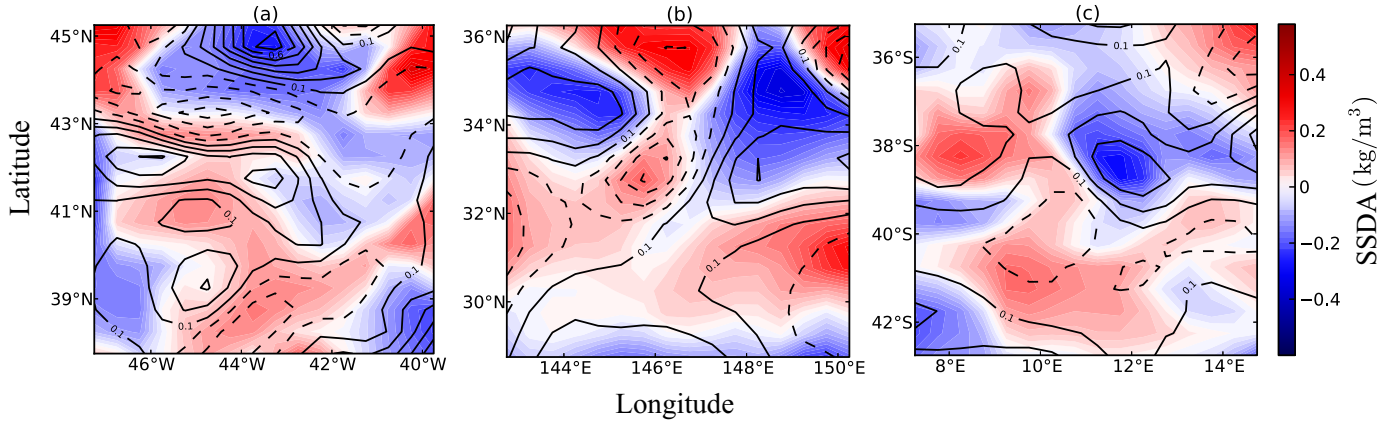

Figure 3. Eddy fields of SSD (color) and SSH (contours) calculated by subtracting the corresponding large-scale background fields from SODA reanalysis data in January 2007 for (a) Gulf Stream region, (b) Kuroshio region, and (c) Agulhas leakage region.

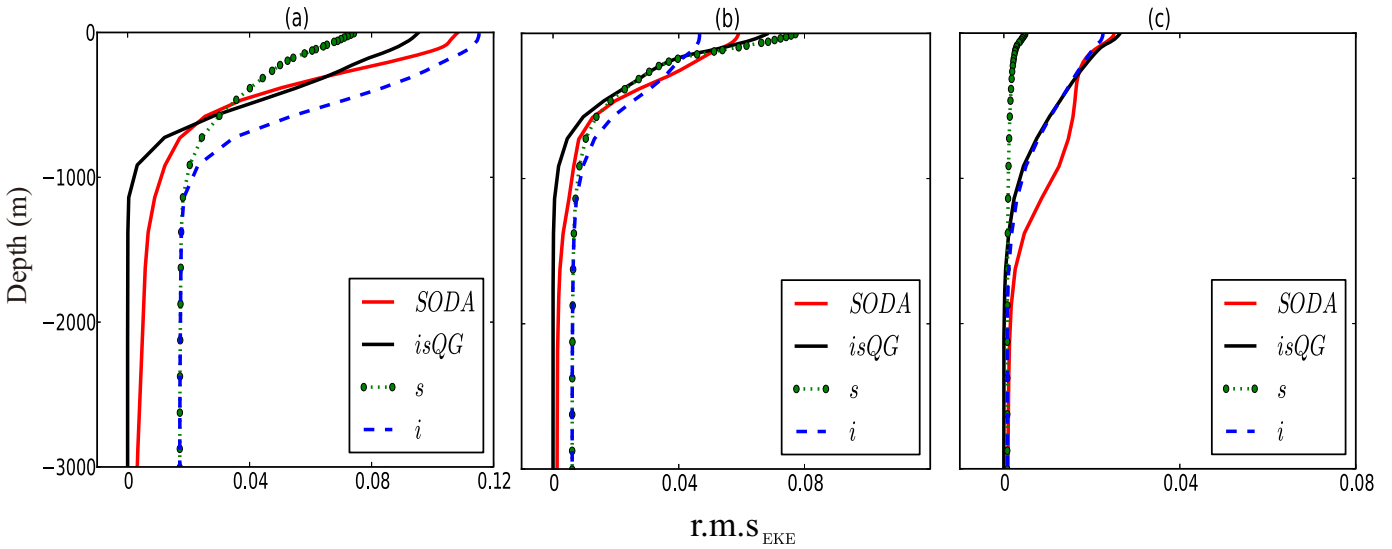

Figure 4. The r.m.s of the perturbation kinetic energy derived from SQG solution (green dotted line), interior solution (blue dashed line), and combined solution (black solid line) and from SODA data (red solid line) for (a) Gulf Stream region, (b) Kuroshio region, and (c) Agulhas leakage region.

field; subscripts *s*, *i*, and *isQG* denote the SQG, interior, and combined isQG solution, respectively; subscript *SODA* refers to the SODA data set, and *HYCOM* represents the HYCOM/NCODA data set.

4.1. Results From SODA Reanalysis

4.1.1. Gulf Stream Extension

The spatial correlation between SSHA and SSDA is weak over this region (Figure 3a), implying that SSD is mostly decoupled from the interior dynamics [*Isern-Fontanet et al*., 2008; *Wang et al*., 2013]. The stratification profile shows two subsurface local maxima, one at the base of the ML, and the other near the main thermocline (Figure 2a).

The vertical profiles of the root-mean-square (r.m.s) of eddy kinetic energy are shown in Figure 4a. The SQG solution contribution (EKE_s, green dotted line) is smaller than the interior solution (EKE_i, blue dashed line) in the upper 1000 m. Combined EKE (EKE_{isQG}, black solid line) of these two solutions matches the SODA data (EKE_{SODA}, red solid line) quite well between −200 and −700 m in the upper layers. In deeper layers, EKE_{isQG} decays a little faster due to the zero-bottom-velocity assumption, which also appears in *Wang et al*. [2013]. According to equation (9), the total stream function at the surface is proportional to the SSH, which means that the surface velocity is set to be geostrophic in the isQG theory. This geostrophic assumption may lead to a discrepancy between EKE_{isQG} and EKE_{SODA} at the surface due to the existence of ageostrophic flows in

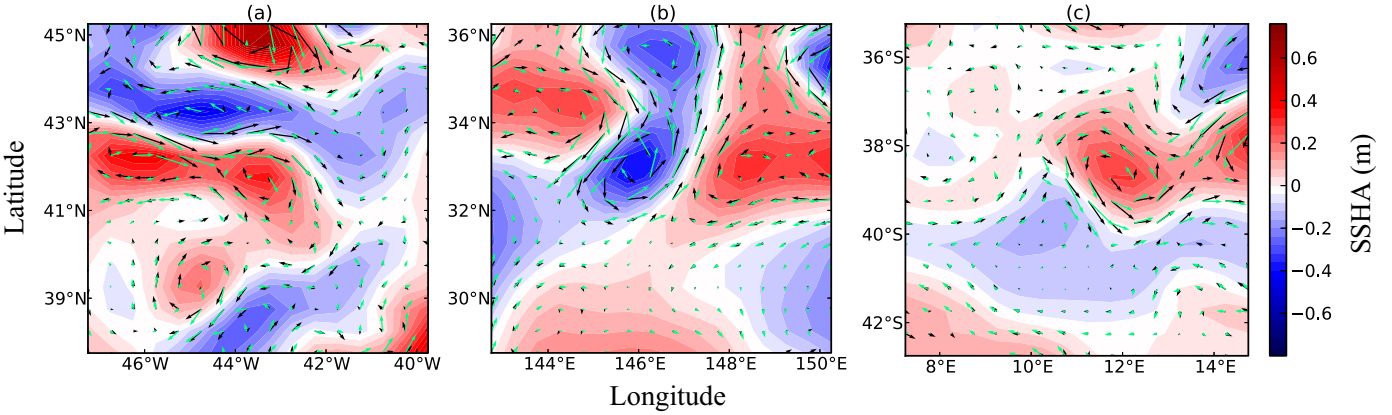

Figure 5. Eddy fields of SSH (color) superimposed with surface velocity perturbation fields derived from SSH (representing geostrophic flows, green arrows) and from SODA data (black arrows), for the region of (a) Gulf Stream, (b) Kuroshio, and (c) Agulhas leakage.

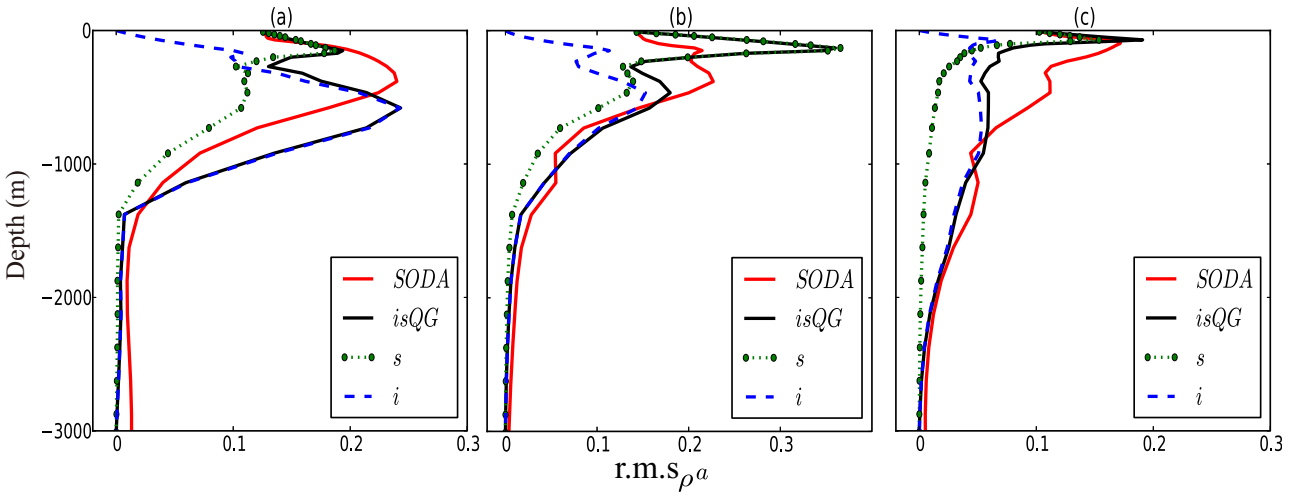

Figure 6. The r.m.s of the eddy density derived from SQG solution (green dotted line), interior solution (blue dashed line), and combined solution (black solid line) and from SODA data (red solid line) for (a) Gulf Stream region, (b) Kuroshio region, and (c) Agulhas leakage region.

this region, as shown in Figure 5a. However, that ageostrophic part does not affect the reconstruction severely, because flows at the surface are generally dominated by the geostrophic part.

Note that the combined EKE_{isQG} includes three terms:

$$EKE_{isQG} = \frac{1}{2}|\vec{V}_s + \vec{V}_i|^2 = EKE_s + EKE_i + \vec{V}_s \cdot \vec{V}_i, \tag{20}$$

$$\text{where} \quad EKE_s = \frac{1}{2}|\vec{V}_s|^2, \qquad EKE_i = \frac{1}{2}|\vec{V}_i|^2. \tag{21}$$

Since the SQG modes and interior QG modes are not orthogonal, the kinetic energy of isQG includes the cross-correlation terms. As seen in Figure 4a, the shape of profiles indicates that the cross-correlation term $\vec{V}_s \cdot \vec{V}_i$ is negative in this case.

The r.m.s of density anomaly from the isQG solution (black solid line in Figure 6a) is similar to that of SODA data (red solid line in Figure 6a), especially above −300 m, where SQG solution (green dotted line in Figure 6a) accounts for a large proportion of the density anomaly. Below −300 m, however, the interior solution (blue dashed line in Figure 6a) dominates and overestimates the true state. The reason could be that the barotropic and first baroclinic modes considered in this study are insufficient to fully represent the interior solution, thus cannot efficiently describe the density variations of SODA data, leading to some inconsistency below −300 m.

Figure 7 shows the density anomalies and the horizontal velocity anomaly vectors from the SODA data and isQG method at three depths. As viewed in the horizontal planes, both the structure and amplitude of isQG fields are very similar to those of SODA fields. In particular, the isQG solution captures all the mesoscale cyclonic and anticyclonic eddies (denoted by C1 and A1–A4 in Figures 7c and 7d) in structure though with difference in magnitude. The density anomaly field retrieved from the isQG method is generally weaker than that from SODA at upper levels (−229 m, −466 m), and is slightly stronger at deeper level (−729 m); the r.m.s density anomaly is shown at the corresponding depth in Figure 6a. For the horizontal velocity anomaly field, the retrieved flows are slightly weaker at −229 and −729 m and stronger at −466 m than those from SODA data.

Table 1 lists the correlation between the isQG solution and the SODA data for the density anomaly and horizontal velocity anomaly fields at three depth levels. The correlation coefficients for the retrieved density anomalies are as high as 0.93 at −466 m and 0.88 at −729 m, indicating good performance in the isQG reconstructed fields. High correlation for the retrieved velocity components is obtained too, with correlation coefficients varying from 0.68 to 0.84 for different layers and different components.

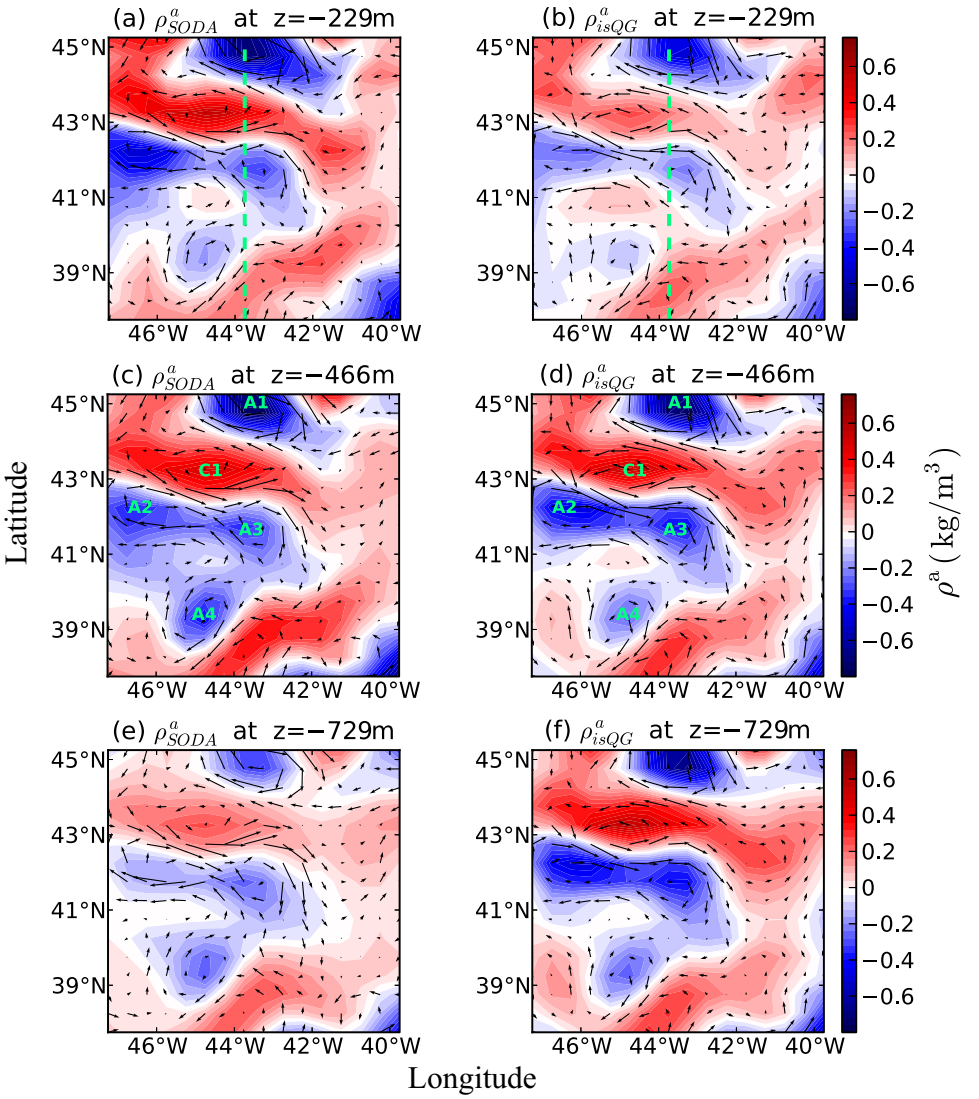

Figure 7. Density anomaly (left) from SODA and (right) from the isQG method at three depths in Gulf Stream region, superimposed with horizontal velocity vectors. The vectors are scaled at different depth, using the corresponding maximum velocity of SODA data and isQG method, respectively. Dashed lines in (a) and (b) mark the location of the vertical section shown in Figure 8. Characters "C" and "A" in (c) and (d) denote cyclonic eddy and anticyclonic eddy, respectively.

Vertical cross section of the density anomaly field at 43.75°W (indicated by dashed line in Figures 7a and 7b) is shown in Figure 8. The SQG solution is surface trapped (Figure 8c), whereas the interior solution reaches its maximum around −600 m (Figure 8d). Only the combination of these two solutions (Figure 8b)

Table 1. Linear Correlation Between Reconstructed isQG Eddy Field and SODA Eddy Field in Three Tested Regions[a]

	Gulf Stream Region			Kuroshio Region			Agulhas Leakage Region		
	−229 m	−466 m	−729 m	−229 m	−466 m	−729 m	−229 m	−466 m	−729 m
Density	0.92	0.93	0.88	0.92	0.96	0.86	0.73	0.67	0.80
Zonal velocity	0.80	0.77	0.68	0.85	0.81	0.72	0.84	0.75	0.58
Meridional velocity	0.84	0.82	0.72	0.89	0.86	0.77	0.86	0.75	0.52
Density(M)	0.96	0.93	0.88	0.95	0.95	0.82	0.79	0.63	0.71
Zonal velocity(M)	0.81	0.80	0.72	0.83	0.82	0.75	0.83	0.78	0.66
Meridional velocity(M)	0.86	0.84	0.75	0.89	0.87	0.79	0.86	0.79	0.59

[a]Variables marked by M denote the results of reconstruction using density anomalies at the base of mixed layer as a proxy of surface values.

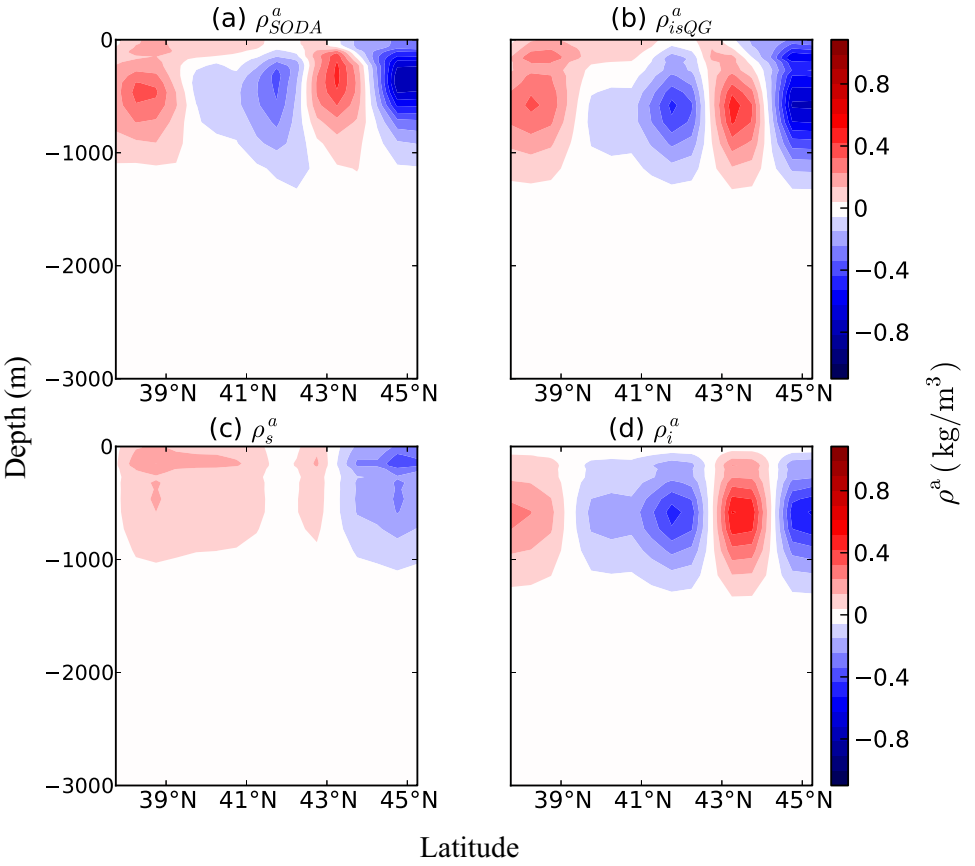

Figure 8. Vertical section of density anomaly at 43.75°W in Gulf Stream region from (a) SODA, (b) isQG combined solution, (c) SQG solution, and (d) interior solution.

can capture the vertical structure of the SODA data (Figure 8a) well, especially the eddy vertical tilt, which cannot be resolved by baroclinic mode or SQG solution alone but is an essential property of baroclinic eddies.

4.1.2. Kuroshio Region

For the Kuroshio region, the SSD and SSH eddy fields are correlated quite well, with some exceptions in the south of the domain (Figure 3b). The stratification also presents two subsurface local maxima (Figure 2b), but is stronger than that in the Gulf Stream region (Figure 2a).

EKE_s is strong in the upper layers, but is a little weaker than EKE_i between −150 m and about −1200 m. The combined EKE_{isQG} correctly reflects the variance in the profile of EKE_{SODA} (Figure 4b). Similar to the region of Gulf Stream extension, obvious discrepancy between EKE_{isQG} and EKE_{SODA} exists at the surface, implying that the ageostrophic velocity at the surface is not negligible (also see Figure 5b).

The r.m.s density anomaly profile demonstrates that the isQG solution well captures the vertical structure in SODA data, especially the two subsurface maxima (Figure 6b). However, the reconstructed magnitude is larger than that of SODA data in the upper 200 m, and is a little smaller below. As the SSDA and SSHA are well correlated and the surface solution accounts for a large portion of the total SSHA variance, the contribution of interior solution is not as prominent below the ML as in the Gulf Stream region (Figure 6a).

Horizontal density anomaly fields are well depicted by the isQG solution in terms of both magnitude and structure, although some small-scale signals are missed (Figure 9). Strong correlation between the retrieved and SODA fields could be found in Table 1, with the highest correlation coefficient of 0.96 at −466 m.

As in the region of Gulf Stream extension, the retrieved horizontal velocity anomalies in the Kuroshio region are qualitatively consistent with SODA data (Figure 9). Most notably, the isQG solution well captures the two mesoscale cyclonic eddies (denoted by C1 and C2 in Figures 9c and 9d), as well as the anticyclonic

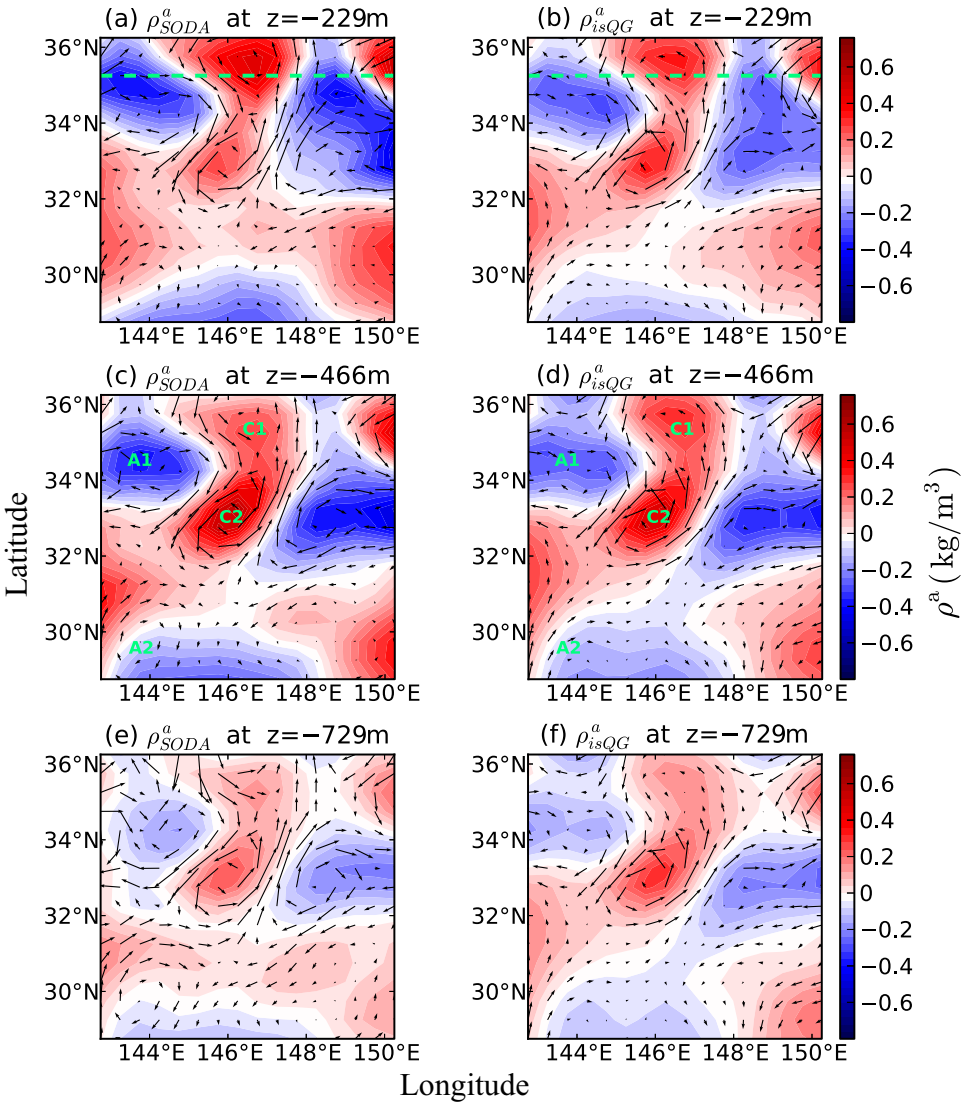

Figure 9. The same as Figure 7, but for Kuroshio region. Dashed lines in (a) and (b) show the location of the vertical section shown in Figure 10.

eddy (denoted by A1 in Figures 9c and 9d), although it does not well capture the relatively weak anticyclonic eddy (denoted by A2 in Figures 9c and 9d). The correlation coefficients between isQG solution and SODA data for the velocity components reach 0.81–0.89 at −229 and −466 m, and 0.72 (0.77) for the zonal (meridional) velocity at −729 m (Table 1).

Figure 10 displays the vertical cross section of density anomalies at 35.25°N (indicated by the dashed line in Figures 9a and 9b). The vertical structures of the eddies in SODA data are well captured by the isQG solution (Figure 10b). The contribution of interior solution (Figure 10d) to the isQG solution is not as notable as that of SQG solution (Figure 10c), indicating the consequence of strong correlation between SSDA and SSHA in this region.

4.1.3. Agulhas Leakage Region

The time we chose for the Agulhas leakage region is local summer. Stratification is strong, with a maximum value approaching $8 \times 10^{-5}\ \mathrm{s}^{-1}$ (Figure 2c), and the correlation between SSDA and SSHA is weak with a correlation coefficient of −0.27 (Figure 3c). We expect the isQG method to be less effective in this region because the decoupling of the SSD with the interior dynamics, as discussed in *Wang et al.* [2013]. This will be an example of the later demonstration that the reconstruction is less satisfactory in summer condition.

It is noticeable that this region is less energetic compared with the two previously mentioned regions (Figure 4), probably because (1) it is in South Hemisphere summer time (January); (2) the SODA data are of relatively

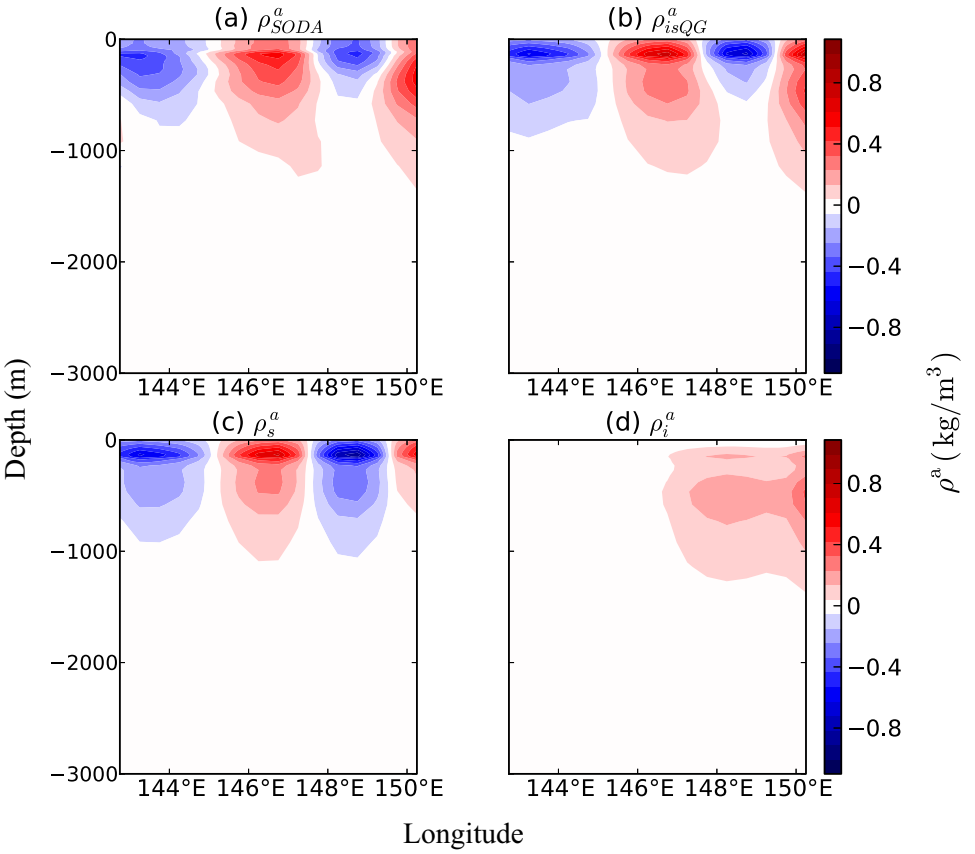

Figure 10. The same as Figure 8, but for Kuroshio region at 35.25°N.

coarse resolution; and/or (3) no Agulhas ring appears in the considered domain of the considered period. EKE_{isQG} matches EKE_{SODA} in the upper 300 m well, but is smaller in the deeper layers (Figure 4c). The consistency between EKE_{isQG} and EKE_{SODA} at the surface suggests that surface flows from SODA reanalysis are nearly geostrophic (also see Figure 5c); however, this does not advance the performance of the isQG reconstruction in the interior ocean, as seen in the discussion below. The retrieved density anomalies also capture the near-surface features of SODA data. However, they decay much faster than those of SODA data around −100 m (Figure 6c).

As shown in Figure 11, the isQG solution generally captures the structures of the density anomalies and horizontal velocity in upper layers (−229 and −466 m), although the retrieved mesoscale anticyclonic eddy (denoted by A1 in Figures 11c and 11d) is relatively weaker, the cyclonic eddy reconstructed (denoted by C1 in Figures 11c and 11d) is slightly shifted northward compared with SODA data, and obvious differences exist between the two velocity fields around 13.5°E, 38.5°S. However, the isQG solution differs noticeably from the SODA data at deeper layers (Figure 11f). The correlation between the isQG solution and the SODA data for the density anomalies and velocity anomalies is slightly low, compared to those in the Gulf Stream extension region and Kuroshio region (Table 1). The poor performance of the isQG method in deeper layers in this region is due to the strong stratification of this region which suppresses the contribution of SQG solution to the isQG solution, as seen in the vertical cross sections of density anomalies (Figure 12). Moreover, using the barotropic mode and the first baroclinic mode alone are not sufficient to fully represent the contribution of interior solution due to the strong stratification in this region. Consequently, the retrieved subsurface fields in this region are not as good as those in regions of the Gulf Stream extension and Kuroshio.

4.2. Results From HYCOM/NCODA Reanalysis

4.2.1. Sensitivity of the isQG Performance to Data Horizontal Resolution

With higher-resolution data set HYCOM/NCODA, the isQG method also shows a satisfactory performance in retrieving the interior fields for the three target regions. As an example, Figure 13 gives the reconstructed density anomaly and velocity anomaly fields at three depths (−250, −500, and −800 m) based on the 1/

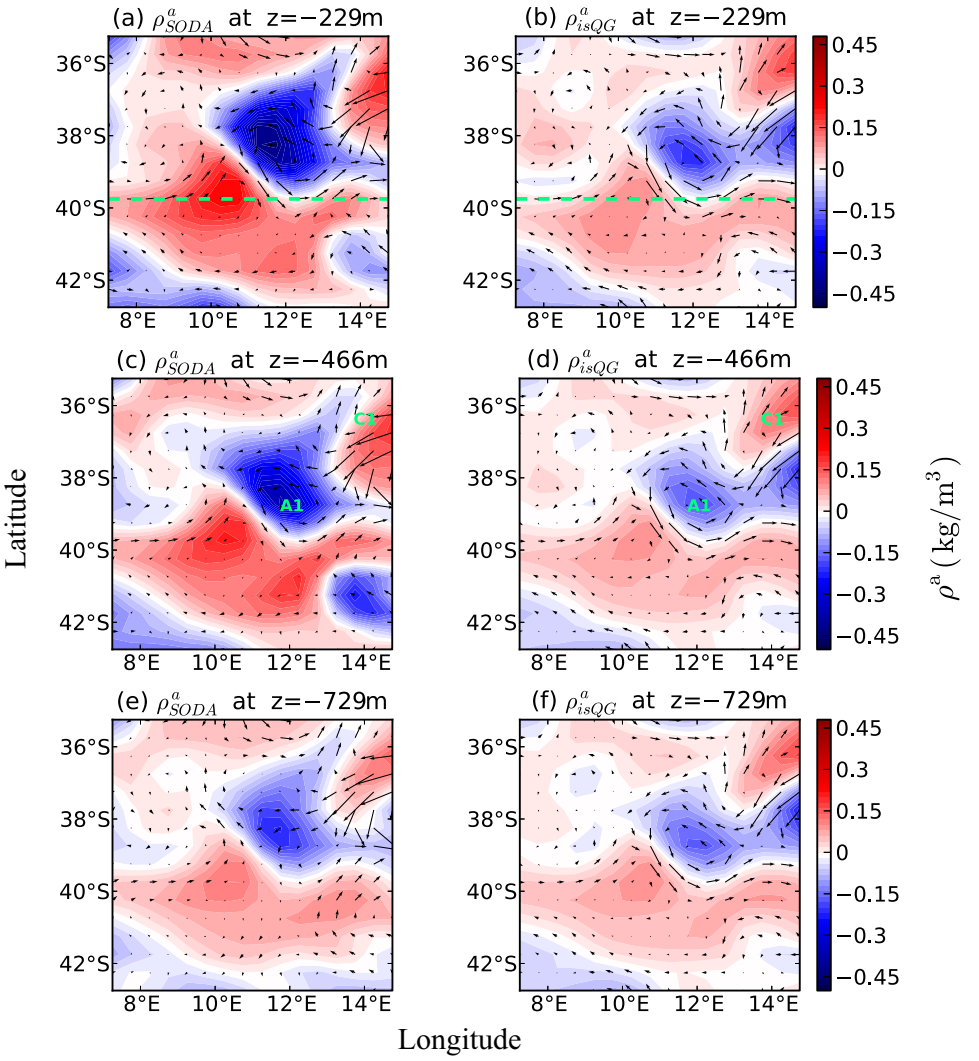

Figure 11. The same as Figure 7, but for Agulhas leakage region. Dashed lines in (a) and (b) show the location of the vertical section shown in Figure 12.

12°-resolution data of January 2010 for the Agulhas leakage region. Good agreement can be seen between the retrieved results and HYCOM/NCODA data, especially the structures of all the mesoscale cyclonic and anticyclonic eddies (denoted by C1 and A1–A4 in Figures 13c and 13d). To investigate the sensitivity of the isQG performance to the horizontal resolution of the same data set, we perform another two reconstructions using coarser resolutions (0.24° and 0.4°) of HYCOM/NCODA data, and compute the correlation between the isQG solution and HYCOM/NCODA data with different resolution for the density anomaly and horizontal velocity anomaly fields (Table 2). The performance of the isQG method degrades significantly for velocity retrieval at all three levels when the resolution gets coarser. For instance, the correlation for the zonal velocity at the depth of −250 m decreases from 0.92 for the 1/12°-resolution to 0.83 for the 0.24°-resolution and to 0.70 for the 0.4°-resolution. On the other hand, the density retrieval is found not as sensitive to the data resolution as the velocity retrieval. Therefore, higher resolution of data can lead to a better isQG performance for the velocity retrieval, but seems have no obvious impact on the density retrieval.

4.2.2. Seasonal Variation of the isQG Performance

Recent studies have found that the temporal evolution of the quality of SQG reconstruction shows obvious seasonal variability (i.e., better performance in winter time than in summer time), which is in agreement with the seasonal variability of the MLD [*González-Haro and Isern-Fontanet*, 2014]. *Wang et al.* [2013] mentioned that the isQG is less effective during summer than the winter, but did not include the results in their paper.

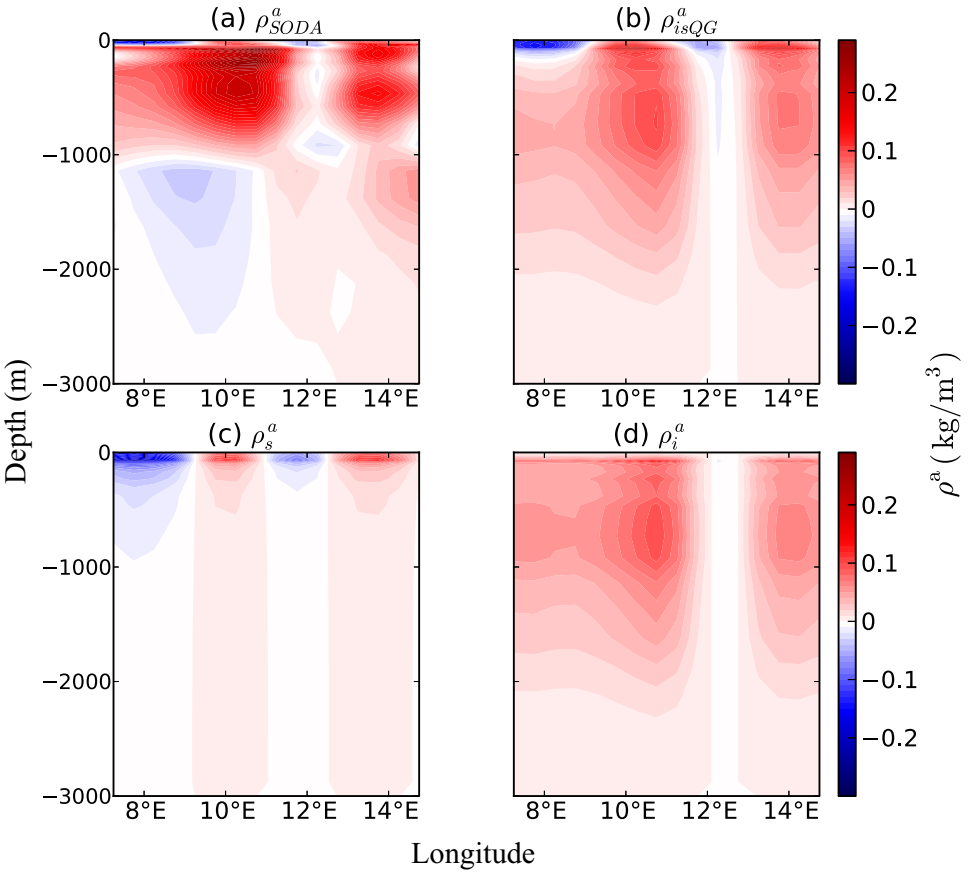

Figure 12. The same as Figure 8, but for Agulhas leakage region at 39.75°S.

Here we investigate the seasonal variation of the isQG performance in reconstructing the ocean's interior in the three target regions using the HYCOM/NCODA data (1/12°) with a time period of 12 months in 2010. To see clearly seasonal variation of the isQG performance, we calculate the mean relative deviation of r.m.s density anomaly between the reconstruction and HYCOM/NCODA data averaged over eight depths (−50, −100, −150, −200, −250, −300, −400, and −500 m) for each month, which is defined as follows:

$$RD_{r.m.s} = \left(\sum_{i}^{N} \left| \frac{r.m.s(i)_{isQG} - r.m.s(i)_{HYCOM}}{r.m.s(i)_{HYCOM}} \right| \right) / _N. \tag{22}$$

Where i is the index of vertical depth and N is the total number of depths (here $N = 8$). It is obvious that $RD_{r.m.s}$is smaller during winter and spring and relatively larger during summer and fall in all the three regions (solid lines in Figure 14). This seasonal variation of the isQG performance may be attributed to that of the upper ocean state. As shown in Figure 14, the MLD (dashed lines in Figures 14a–14c) presents large values in winter and early spring corresponding to weaker stratification represented by smaller maximum values of N^2 (dashed lines in Figures 14d–14f). The ML begins to shoal in late spring and maintains a relatively shallower depth during summer and fall with a stronger stratification. Deep ML and weak stratification during winter enhance the penetration of SQG solution. Recent studies showed that the phase shift between SST and SSH is minimum (i.e., maximum correlation between SST and SSH) for deep ML [*Isern-Fontanet et al.*, 2008, 2014]. Less phase shift between SSTA and SSHA leads to a good performance of the isQG method. The strong anticorrelation between SSHA and SSDA in winter months (dashed lines in Figures 14g–14i) implies that the density of the surface layer couples with interior dynamics quite well and the SSH signals are largely attributed to the SQG solution, making the bias of the two-gravest-mode-only interior solution less dominant in the total resolution of the reconstruction. However, the mean surface density anomaly gradient ($\nabla SSDA$, dashed lines in Figures 14j–14l) shows no evident seasonal signal, and consequently exerts less influence on the seasonal variation of the isQG retrieval.

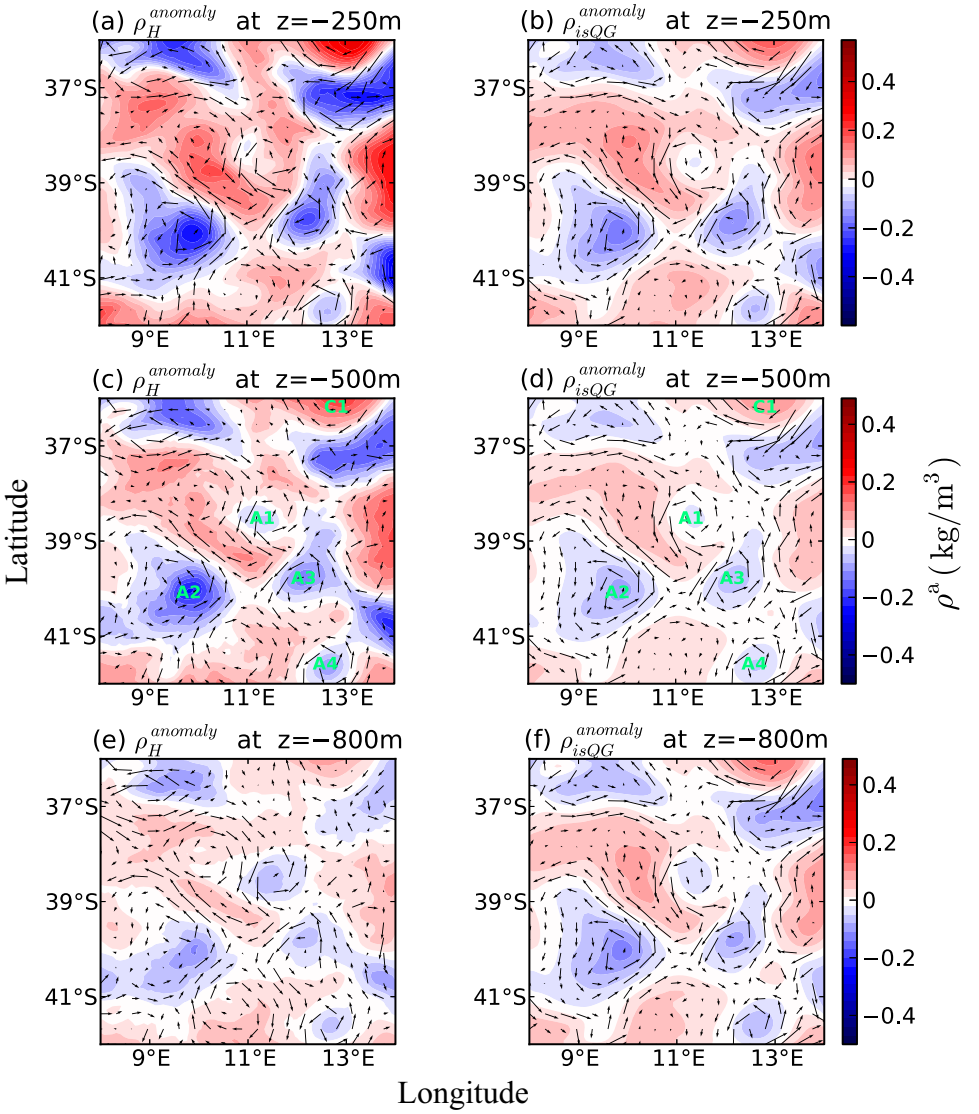

Figure 13. The same as Figure 7, but for the case of 1/12°-resolution HYCOM/NCODA data (January 2010) in Agulhas leakage region.

Therefore, the seasonal variations of the MLD, stratification and correlation between SSHA and SSDA are the major factors causing the seasonal variation of the isQG performance in reconstructing the ocean's interior, i.e., better performance during winter and spring than during summer and fall.

5. Summary and Discussion

In this paper, we employ two reanalysis data sets (SODA and HYCOM /NCODA) to further validate the isQG method for reconstructing the ocean interior from sea surface information (density and height) and the

Table 2. Linear Correlation Between Reconstructed isQG Eddy Field and HYCOM Eddy Field for Three Horizontal Resolutions in the Region of Agulhas Leakage

	1/12°			0.24°			0.4°		
	−250 m	−500 m	−800 m	−250 m	−500 m	−800 m	−250 m	−500 m	−800 m
Density	0.93	0.92	0.83	0.93	0.93	0.83	0.93	0.93	0.83
Zonal velocity	0.92	0.81	0.65	0.83	0.73	0.59	0.70	0.60	0.47
Meridional velocity	0.94	0.80	0.64	0.89	0.75	0.60	0.79	0.66	0.52

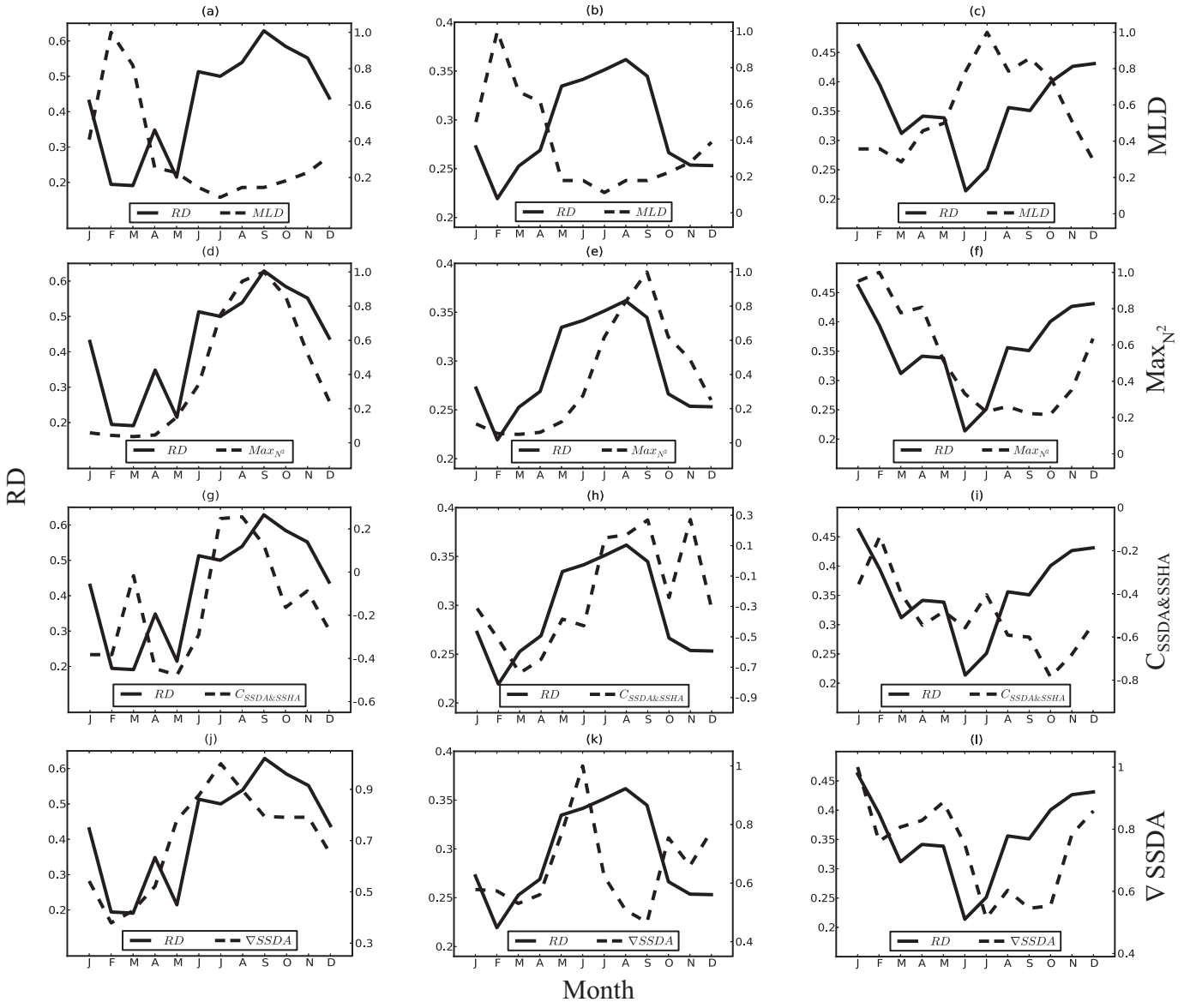

Figure 14. Monthly variations of mean relative deviations of r.m.s density anomaly between the reconstruction and HYCOM/NCODA data (solid lines), and the corresponding variations of mixed layer depth (dashed lines in the first row), maximum value of stratification (dashed lines in the second row), correlation coefficient between SSDA and SSHA (dashed lines in the third row), mean surface density anomaly gradient (dashed lines in the fourth row) from January 2010 to December 2010 for the regions of (left) Gulf Stream extension, (middle) Kuroshio, and (right) Agulhas leakage. The mean relative deviations of r.m.s density anomaly are computed as the ratio of the r.m.s density anomaly difference between the reconstruction and HYCOM/NCODA data to the r.m.s density anomaly of the HYCOM/NCODA data and averaged over eight depths (−50, −100, −150, −200, −250, −300, −400, and −500 m). The mixed layer depth, maximum value of stratification, and surface density anomaly gradient are scaled by their maximum values, respectively, i.e., 275 m, 40.63×10^{-5} s^{-1}, 4.6×10^{-6} kg m^{-4} for (left) Gulf Stream extension; 225 m, 57.77×10^{-5} s^{-1}, 4.4×10^{-6} kg m^{-4} for (middle) Kuroshio; and 175 m, 13.92×10^{-5} s^{-1}, 4.0×10^{-6} kg m^{-4} for (right) Agulhas leakage.

vertical stratification only, as well as to investigate the seasonal variation of the isQG performance and its sensitivity to the data resolution. Our results indicate that the isQG method is robust in retrieving the ocean interior from sea surface information with better performance in winter than in summer, and higher-resolution data are beneficial for the velocity retrieval.

The validation is performed in three regions, i.e., the Gulf Stream extension, the Kuroshio system east off Japan, and the Agulhas leakage in the South Atlantic Ocean. In general, density anomaly and velocity anomaly fields in the upper 1000 m depth are successfully retrieved by the isQG method in all these regions. In particular, the structure of the mesoscale eddies represented in the horizontal density anomaly field or the velocity anomaly field is well captured by the isQG solution, especially in the regions of the Gulf Stream extension and the Kuroshio system.

The best performance of the isQG method in the energetic Kuroshio region may be attributed to the high correlation between SSDA and SSHA fields and the strong SQG signals, although the stratification here is strong. In the Gulf Stream region and Agulhas leakage region, however, the correlation between SSDA field and SSHA field is poor; this may be partially due to strong influence of the atmospheric forcing on the SSD, which further decouples the surface density signal from the interior dynamics. In such cases, the SSHA field mostly reflects interior dynamics, and the contribution of interior solution below the ML is dominant. Nevertheless, the reconstruction in the Gulf Stream region is still satisfactory, probably attributed to its strong SQG signals and its weak stratification which allows the SQG signals penetrating into the deeper layers. The Agulhas leakage region is different from the Gulf Stream region with weak SQG signals (less energetic, probably due to the relatively coarse resolution of SODA data or other reason as addressed in section 4.1.3) and strong stratification. The strong stratification may suppress the vertical penetration of the already weak SSDA signal into deeper layers, resulting in less contribution of the SQG solution to the isQG solution and thus less satisfactory reconstruction in deeper layers in this region. Moreover, due to the strong baroclinic feature with high stratification in this region, only using these two gravest modes (i.e., the barotropic mode and the first baroclinic mode) may be not sufficient to fully capture the structure of the upper ocean. Therefore, including higher baroclinic modes may further improve the reconstruction in regions where strong stratification exists.

Besides the spatial variation, seasonal variation of the performance of the isQG method exits. Generally speaking, isQG method is more effective during winter and spring when the ML is deeper with weaker stratification, while it is slightly degraded during summer and fall with shallower ML and stronger stratification.

The investigation on the sensitivity of the isQG performance to the data resolution indicates that, for the velocity retrieval, the isQG method performs better with higher data resolution than with coarser data resolution, although the density retrieval seems not as sensitive to the data resolution as the velocity retrieval. This result suggests that we should use sea surface data (including SST, SSS and SSH) with higher resolution when implementing the isQG method to reconstruct the interior ocean.

As addressed by *Isern-Fontanet et al.* [2008], the SQG reconstruction can be most successful when the SST resembles the density anomaly at the base of the ML, which means that using density anomalies at the base of the ML as input of the SQG reconstruction is the best choice. To check if this is valid for the isQG method, we have also performed the reconstruction using the isQG method and density anomalies from SODA reanalysis at the base of the ML as a proxy of the surface value. As shown in Table 1, a more successful reconstruction is achieved with higher correlation (especially for the velocity retrieval) when using density anomalies at the base of the ML, compared to the reconstruction using density anomalies at the sea surface. However, in practice, because satellites usually only provide observations at the sea surface instead of at the base of the ML, the isQG method is thus designed for making use of sea surface data from satellites, i.e., the SST, SSS, and SSH.

Our results here are encouraging, and a step forward is to reconstruct the ocean's interior from the satellite-derived SSH, SST, and SSS data using the isQG method. We will further validate this method in a real ocean situation using satellite-derived sea surface data, including the surface salinity data from SMOS/Aquarius and in situ subsurface observations. In addition, we will try to add more eigenmodes besides the barotropic mode and the first baroclinic mode in the interior solution to further improve the reconstruction.

Acknowledgments
We are grateful to the freely available SODA assimilation data set (https://climatedataguide.ucar.edu/climate-data/soda-simple-ocean-data-assimilation) and the HYCOM/NCODA data set (http://hycom.org/dataserver). This work was jointly supported by the MOST of China (grant 2011CB403505 & 2014CB953904), the China Special Fund for Meteorological Research in the Public Interest (NO. GYHY201406008), the Strategic Priority Research Program of the Chinese Academy of Sciences (grant XDA11010304), National Natural Science Foundation of China (grant 41376021). J. Wang is supported by the National Science Foundation (NSF) through grant OCE-1234473. We would like to thank the anonymous reviewers for their valuable and helpful comments.

References

Bishop, C. H., and A. J. Thorpe (1994), Potential vorticity and the electrostatics analogy: Quasi-geostrophic theory, *Q. J. R. Meteorol. Soc.*, *120*, 713–731.

Blumen, W. (1978), Uniform potential vorticity flow. Part I: Theory of wave interactions and two-dimensional turbulence, *J. Atmos. Sci.*, *35*, 774–783.

Carnes, M. R., J. L. Mitchell, and P. W. deWitt (1990), Synthetic temperature profiles derived from Geosat altimetry: Comparison with air-dropped expendable bathythermograph profiles, *J. Geophys. Res.*, *95*, 17,979–17,992.

Carnes, M. R., W. J. Teague, and J. L. Mitchell (1994), Inference of subsurface thermohaline structure from fields measurable by satellite, *J. Atmos. Oceanic Technol.*, *11*, 551–566.

Carton, J. A., and B. S. Giese (2008), A reanalysis of ocean climate using Simple Ocean Data Assimilation (SODA), *Mon. Weather Rev.*, *136*, 2999–3017.

Charney, J. G., and G. R. Flierl (1981), Oceanic analogues of large-scale atmospheric motions, in *Evolution of Physical Oceanography*, edited by B. Warren and C. Wunsch, pp. 504–548, MIT Press, Mass.

Chassignet, E. P., et al. (2009), U. S. GODAE: Global ocean prediction with the Hybrid Coordinate Ocean Model (HYCOM), *Oceanography*, *22*, 64–75.

Chelton, D. B., M. G. Schlax, and R. M. Samelson (2011), Global observations of nonlinear mesoscale eddies, *Prog. Oceanogr.*, *91*, 167–216.
Chen, D., S. E. Zebiak, and M. A. Cane (1997), Initialization and predictability of a coupled ENSO forecast model, *Mon. Weather Rev.*, *125*, 773–788.
Cooper, M., and K. Haines (1996), Altimetric assimilation with water property conservation, *J. Geophys. Res.*, *101*, 1059–1077, doi:10.1029/95JC02902.
Cummings, J. A. (2005), Operational multivariate ocean data assimilation, *Q. J. R. Meteorol. Soc.*, *131*, 3583–3604, doi:10.1256/qj.05.105.
Ferrari, R., and C. Wunsch (2010), The distribution of eddy kinetic and potential energies in the global ocean, *Tellus, Ser. A*, *62*, 92–108.
Fofonoff, N. P., and R. C. Millard Jr. (1983), UNESCO technical papers in marine science: Algorithms for computation of fundamental properties of seawater, *Rep. 44*, U. N. Educ. Sci. and Cult. Organ., Paris.
González-Haro, C., and J. Isern-Fontanet (2014), Global ocean current reconstruction from altimetric and microwave SST measurements, *J. Geophys. Res. Oceans*, *119*, 3378–3391, doi:10.1002/2013JC009728.
Haines, K. (1991), A direct method for assimilating sea surface height data into ocean models with adjustments to the deep circulation, *J. Phys. Oceanogr.*, *21*, 843–868.
Hakim, G. J., C. Snyder, and D. J. Muraki (2002), A new surface model for cyclone-anticyclone asymmetry, *J. Atmos. Sci.*, *59*, 2405–2420.
Held, I. M., R. T. Pierrehumbert, S. T. Garner, and K. L. Swanson (1995), Surface quasigeostrophic dynamics, *J. Fluid Mech.*, *282*, 1–20.
Hoskins, B. J. (1975), The geostrophic momentum approximation and the semi-geostrophic equations, *J. Atmos. Sci.*, *32*, 233–242.
Hoskins, B. J., M. E. McIntyre and A. W. Robertson (1985), On the use and significance of isentropic potential vorticity maps, *Q. J. R. Meteorol. Soc.*, *110*, 877–946.
Hurlburt, H. E. (1986), Dynamic transfer of simulated altimeter data into subsurface information by a numerical ocean model, *J. Geophys. Res.*, *91*, 2372–2400.
Isern-Fontanet, J., B. Chapron, G. Lapeyre, and P. Klein (2006), Potential use of microwave sea surface temperatures for the estimation of ocean currents, *Geophys. Res. Lett.*, *33*, L24608, doi:10.1029/2006GL027801.
Isern-Fontanet, J., G. Lapeyre, P. Klein, B. Chapron, and M. W. Hecht (2008), Three dimensional reconstruction of oceanic mesoscale currents from surface information, *J. Geophys. Res.*, *113*, C09005, doi:10.1029/2007JC004692.
Isern-Fontanet, J., M. Shinde, and C. González-Haro (2014), On the transfer function between surface fields and the geostrophic stream function in the Mediterranean Sea, *J. Phys. Oceanogr.*, *44*, 1406–1423, doi:10.1175/JPO-D-13-0186.1.
Juckes, M. (1994), Quasigeostrophic dynamics of the tropopause, *J. Atmos. Sci.*, *51*, 2756–2768.
Klein, P., B. L. Hua, G. Lapeyre, X. Capet, S. L. Gentil, and H. Sasaki (2008), Upper ocean turbulence from high-resolution 3D simulations, *J. Phys. Oceanogr.*, *38*, 1748–1763.
Klein, P., J. Isern-Fontanet, G. Lapeyre, G. Roullet, E. Danioux, B. Chapron, S. Le Gentil, and H. Sasaki (2009), Diagnosis of vertical velocities in the upper ocean from high resolution sea surface height, *Geophys. Res. Lett.*, *36*, L12603, doi:10.1029/2009GL038359.
LaCasce, J. H. (2012), Surface quasigeostrophic solutions and baroclinic modes with exponential stratification, *J. Phys. Oceanogr.*, *42*, 569–580.
LaCasce, J. H., and A. Mahadevan (2006), Estimating subsurface horizontal and vertical velocities from sea surface temperature, *J. Mar. Res.*, *64*, 695–721.
Lapeyre, G., and P. Klein (2006), Dynamics of the upper oceanic layers in terms of surface quasigeostrophy theory, *J. Phys. Oceanogr.*, *36*, 165–176.
Pedlosky, J. (1987), *Geophysical Fluid Dynamics*, Springer, N. Y.
Rosati, A., K. Miyakoda, and R. Gudgel (1997), The impact of ocean initial conditions on ENSO forecasting with a coupled model, *Mon. Weather Rev.*, *125*, 754–772.
Smith, K. S., and G. K. Vallis (2001), The scales and equilibration of midocean eddies: Freely evolving flow, *J. Phys. Oceanogr.*, *31*, 554–571.
Stammer, D. (1997), Global characteristics of ocean variability estimated from regional TOPEX/POSEIDON altimeter measurements, *J. Phys. Oceanogr.*, *27*, 1743–1769.
Syu, H.-H., and D. Neelin (2000), ENSO in a hybrid coupled model. Part II: Prediction with piggyback data assimilation, *Clim. Dyn.*, *16*, 35–48.
Tang, Y., and W. W. Hsieh (2003), ENSO simulation and prediction in a hybrid coupled model with data assimilation, *J. Meteor. Soc. Jpn.*, *81*, 1–19.
Tulloch, R., and K. S. Smith (2006), A theory for the atmospheric energy spectrum: Depth-limited temperature anomalies at the tropopause, *Proc. Natl. Acad. Sci. U. S. A.*, *51*, 2756–2768.
Tulloch, R., and K. S. Smith (2009), Quasigeostrophic turbulence with explicit surface dynamics: Application to the atmospheric energy spectrum, *J. Atmos. Sci.*, *66*, 450–467.
Wang, J., G. Flierl, J. LaCasce, J. McClean, and A. Mahadevan (2013), Reconstructing the ocean's interior from surface data, *J. Phys. Oceanogr.*, *43*, 1611–1626, doi:10.1175/JPO-D-12-0204.1.
Watts, D. R., C. Sun, and S. Rintoul (2001), A two-dimensional gravest empirical mode determined from hydrographic observations in the Subantarctic Front, *J. Phys. Oceanogr.*, *31*, 554–571.
Wunsch, C. (1997), The vertical partition of oceanic horizontal kinetic energy, *J. Phys. Oceanogr.*, *27*, 1770–1794.